Acceleration of ions and nano dust at a comet in the solar wind

H. Gunell[a], I. Mann[b,c], C. Simon Wedlund[d], E. Kallio[d], M. Alho[d], H. Nilsson[e], J. De Keyser[a], F. Dhooghe[a], R. Maggiolo[a]

[a]*Belgian Institute for Space Aeronomy, Avenue Circulaire 3, Brussels, Belgium*
[b]EISCAT *Scientific Association, Kiruna, Sweden*
[c]*Physics Department, Umeå University, Umeå, Sweden*
[d]*Aalto University, School of Electrical Engineering, Department of Radio Science and Engineering, Espoo, Finland*
[e]*Swedish Institute of Space Physics, Kiruna, Sweden*

Abstract

A quasi-neutral hybrid simulation of the interaction of the solar wind with the atmosphere of a comet is used together with a test particle simulation of cometary ions and dust to compute trajectories and velocity distribution functions of charged particles, starting outside the diamagnetic cavity at 150 km cometocentric distance. The simulations are run with parameters suited to make predictions for comet 67P/Churyumov-Gerasimenko when it is at a heliocentric distance of 1.45 AU. It is found that the shape of the ion trajectories depends on the location of the source, and that a velocity distribution that is observed at a given point in space is influenced by the spatial structure of the source. Charged dust grains with radii in the $1-10$ nm range are accelerated from the nucleus to a distance of 2.9×10^4 km in between 15 minutes and 2 hours approximately. Dust particles smaller than 10 nm in radius are accelerated to speeds over 10 km/s.

Keywords: comet, dust, hybrid model

---

1. Introduction

As a comet approaches perihelion and comes closer to the sun, the sublimation of volatiles leads to ejection of gas, ice, and dust. When the water sublimation temperature is reached, it releases a huge amount of water that is ionised by ultraviolet photons from the sun and through charge exchange with the solar wind protons. Observations at comet Giacobini-Zinner showed water-group ion distribution functions that followed a power law at high energies and were flattened at low energies (Richardson et al., 1987). Recent observations by the Rosetta spacecraft at comet 67P/Churyumov-Gerasimenko (Nilsson et al., 2015a) showed how the newly created H_2O^+ ions are picked up by the solar wind and accelerated away from the cometary nucleus in the direction of the solar wind electric field. These observations took place in the early stages of the formation of a cometary magnetosphere when a diamagnetic cavity had not yet been established, while the comet was at heliocentric distances between 3.3 and 3.6 astronomical units (AU), and with the spacecraft between 28 and 100 km from the cometary nucleus.

The cometary pickup ions have been seen to undergo pitch angle scattering into shell-like distributions at comets Halley (Coates et al., 1989) and Grigg-Skjellerup (Coates et al., 1993). These observations were made at distances on the order of 10^5 and 10^6 km from the comet at Grigg-Skjellerup and Halley respectively, when each comet had developed its diamagnetic cavity. This means that the length scales involved in the scattering are those of Alfvén waves and MHD. Fluctuations at smaller scales may also occur in the cometary environment as a result of various different plasma instabilities, such as the Kelvin-Helmholtz instability (Chandrasekar, 1961) or the modified two-stream instability (McBride et al., 1972; Raadu, 1978). In the vicinity of Mars, where the solar wind interacts with the ionosphere of the planet as well as with its neutral exosphere, oscillations in the millihertz range have been observed (Winningham et al., 2006; Gunell et al., 2008). Also mirror mode waves have been suggested as a source of fluctuations at comets (Schmid et al., 2014).

The constituent of comets that most easily can be seen from the ground is a large dust grain population, in the micro-metre size range. These grains move under the influence of the sun's radiation pressure (Eddington, 1910). Schulz et al. (2015) observed dust grains up to a size of 500 μm using the COSIMA instrument on the Rosetta spacecraft. Rotundi et al. (2015) found dust grains in the 100 μm to millimetre range to be more effective optical scatterers than those in the micrometre range when 67P/Churyumov-Gerasimenko was between 3.7 and 3.4 AU from the sun, but they expected that to change as the distance from comet to sun decreases. The reason for this expectation is an asymmetry in the grain size distribution between the northern and southern halves of the

---

Email address: `herbert.gunell@physics.org` (H. Gunell)

nucleus, leading to an increase of the emission of small grains from the southern side starting at about 2 AU (Fulle et al., 2010). For dust particles in the size range of tens of nanometres or smaller – that is to say, the nano dust – the scattering cross sections are small and these dust particles do not contribute much to visual observations. As a result the radiation pressure force is also small and instead electrostatic forces become increasingly important. The drag force from the neutral gas is also an important force on the dust grains, but only within a few kilometres from the nucleus.

Snios et al. (2014) compared observations of hard X-rays from five comets with models of scattering and fluorescence of X-rays originating at the sun. They found that scattering by cometary gas was insufficient to explain the observed intensities and suggested that the observations could be explained by scattering from dust particles, both large, in the micro-metre range, and small nanometre sized particles. Szego et al. (2014) predicted that nano dust at comet 67P/Churyumov-Gerasimenko could be observed by the ion and electron sensor (IES) on board the Rosetta spacecraft. Dust particles, down to 2 nm in size, from Saturn's E-ring can be accelerated and ejected from Saturn's magnetosphere and are observed as "Saturnian stream particles" (Hsu et al., 2011). Dust composition and dynamics at both Saturn and Jupiter were reviewed by Hsu et al. (2012). It is not clear how nanometre-sized dust can be lifted from the surface of the comet, but some evidence for the existence for nano dust was already observed with Giotto near comet Halley (Utterback and Kissel, 1990, 1995). In contrast to the nano dust near planets, mentioned above, that possibly originates from a condensation process, the dust near the comet is possibly due to fragmentation, see discussion by Mann and Czechowski (2012). Several observations suggest that dust fragmentation events occur near the comet – discussed by Mann et al. (2006) – so that small dust particles can be produced independent from the conditions of leaving the nucleus. And for instance Clark et al. (2004) discuss fragmentation in order to explain the unpredicted heterogeneity in particle number density that they observed in the coma of Wild 2.

In this paper we present results from a simulation meant to model comet 67P/Churyumov-Gerasimenko when it is at a solar distance of 1.45 AU. We compute distribution functions for cometary water ions. We study the effect the size of the ion source region has on these distributions, and we examine the effects of electric field fluctuations in a region along the ion trajectory. We use the same approach to compute trajectories of dust grains in the size range from 1 to 10 nm, and analyse how the acceleration depends on the dust grain size. The simulation model is described in Section 2; ion distribution functions are presented in Section 3; trajectories of nano dust are computed in Section 4; and the conclusions are discussed in Section 5.

2. Model

The simulations are performed in two steps. First, a global quasi-neutral hybrid model is used to produce electric and magnetic fields. Second, test particle simulations are run, using the calculated fields to compute trajectories for ions and dust particles.

2.1. Quasi-neutral hybrid model

The 3-D self-consistent global plasma simulations were performed using a model based on the hybrid modelling platform HYB, now developed at Aalto University (Finland) and applied to a cometary environment. The model describes the plasma using the quasi-neutral hybrid approach, treating ions as kinetic particles and electrons as a charge-neutralising massless fluid so that $\sum_i \; q_i \; n_i + q_e \; n_e = 0$ where q_i, n_i and q_e, n_e are the ion charge and density and electron charge and density, respectively. The model has been tested for more than 15 years and has been used to study the interaction between the solar wind and planetary objects, such as Mars and Venus (e.g., Jarvinen et al., 2014), the Moon (Kallio, 2005) or, more recently, comets such as comet C/2013 A1 "Siding Spring" for which solar wind mass-loading simulations were performed (Gronoff et al., 2014). The model was described in detail in, e.g., Kallio and Janhunen (2003), Kallio et al. (2006), Kallio and Jarvinen (2012); only specifics related to the electromagnetic fields and inputs for the simulation are provided here. The ion dynamics is governed by the Lorentz force in the expression of Newton's second law, while the electrodynamics fields $(\mathbf{E}, \mathbf{B})$ are solved by Ampère's and Faraday's laws. Ions are accelerated by the Lorenz force where the electric field is derived from $\mathbf{E} + \mathbf{U_e} \times \mathbf{B} = 0$, where $\mathbf{U}_e$ is the electron bulk velocity. Finite ion gyromotion effects and Hall term are naturally included, giving rise to kinetic effects and plasma asymmetries. In the hybrid model, electron resistivity is included in the propagation of the magnetic field in time by Faraday's law $\partial \mathbf{B}/\partial t = -\nabla \times \mathbf{E} = -\nabla \times (-\mathbf{U}_\mathrm{e} \times \mathbf{B} + \eta \mathbf{j})$; after several values were tested, a conservative value of $\eta = 0.02\ \Omega\,\mathrm{m}$ was found to yield more stable results and sharper boundaries than in the case of $\eta = 0$. Moreover, the electron pressure term was ignored since our tests showed that it did not significantly affect the final calculated electromagnetic fields at the spatial scales considered. Grid refinement techniques can be used to target a specific area of the object's environment.

To perform the 3-D global hybrid plasma simulations, a neutral model of the cometary coma is first needed. We used the classical spherically-symmetric expansion model of Haser (1957):

$$n_n(r) = \frac{Q}{4\pi r^2 V} e^{-r/\lambda_{\mathrm{H_2O}}} \qquad (1)$$

where Q is the production rate of neutral species ejected from the comet under the action of the Solar radiation (in

Table 1: Neutral parameters for the Haser model of comet 67P/Churyumov-Gerasimenko at 1.45 AU. $Q(H_2O)$ is the neutral H_2O outgassing rate from the comet, V the velocity of the expanding neutral cloud, λ_{H_2O} the total photodestruction scale length at 1.45 AU heliocentric distance, including ionisation and dissociation and at low solar activity.

$Q(H_2O)$ [s^{-1}]	V [km s^{-1}]	λ_{H_2O} [km]
2.36×10^{27}	0.70	1.22×10^5

our case H_2O), r the cometocentric distance, V the velocity of the escaping neutrals and λ_{H_2O} the photodestruction scale length (estimated from the photo-rates given by Huebner et al. (1992) for H_2O). Parameters for the Haser neutral model are collected in Table 1. Photodissociation of H_2O into H is negligible below 3×10^4 km from the nucleus, where charge exchange processes between the solar wind and the cometary neutrals may become dominant.

The parameters of the upstream solar wind as well as the photo-ion production rate are summarised in Table 2. The upstream parameters correspond to the conditions recommended by Hansen et al. (2007) propagated at 1.45 AU, i.e., close to perihelion, and hence representing common values expected by Rosetta at comet 67P/Churyumov-Gerasimenko. The solar wind is composed of protons H^+ and alpha particles He^{2+}, the latter amounting to 4% of the proton density. Charge transfer reactions between the solar wind particles and H_2O cometary molecules significantly affect the mass loading and the magnetic field morphology upstream and downstream of the nucleus. A simple analytic model (see Nilsson et al., 2015a, appendix) shows that, when compared to charge transfer with He^{2+}, charge transfer with H^+ plays the major role at the resolution used in the hybrid runs ($\sim$ 300 km) in removing mass and momentum from the flow. $H^+ - H_2O$ charge transfer cross section at 400 km s^{-1} is 1.8×10^{-19} m^2 (Lindsay et al., 1997). Electron impact ionisation is expected to be no more than an order of magnitude less efficient than charge exchange processes but it is not considered here for simplicity. With these parameters, the model reaches a steady state after about 300 s.

Fig. 1 presents the results of the 3-D global hybrid-neutral plasma simulations in the following coordinate system: the solar wind moves towards $-x$, the interplanetary magnetic field, perpendicular to the flow of the solar wind, is in the $+y$ direction, while the z axis completes the right-hand coordinate system. Since cometary ions picked up by the solar wind predominantly move in the $x-z$ plane, we chose this plane for representing the physical quantities. The comet is situated at $(x, y, z) = (0, 0, 0)$ and the simulation box size in x, y and z directions is $\pm 3 \times 10^4$ km. The size of the grid cells is $\sim$ 300 km close to the nucleus and $\sim$ 1200 km near the boundaries of the simulation box. This means that the diamagnetic cavity is not resolved, and that we only consider phenomena that occur outside it. In Fig. 1(a) and (b), we have plotted the magnetic field B_y and electric field E_z components. Fig. 1c shows H_2O^+ ions: originally created by photoionisation of cometary H_2O molecules and from charge transfer with H^+ solar wind ions, they are then picked up and accelerated towards the $+z$ direction following the convection electric field $-U_x^{sw} \times B_y$, forming a typical cometary tail of escaping ions. The density of H_2O^+ ions is of the same order of magnitude as that of the solar wind protons, with densities reaching a few times 10^7 ions m^{-3} at cometocentric distances less than 1000 km as seen in Fig. 1f.

This simulation shows a classic case of solar wind mass-loading, with the interplanetary magnetic field being mostly undisturbed upstream of the comet. A bow shock appears upstream of the nucleus, with a subsolar stand-off distance on the order of 2×10^3 km, as shown in panels (d) and (e) of Fig. 1, representing a close-up of the magnetic and electric fields close to the comet nucleus. This is in accordance with previous simulations at perihelion (e.g., Koenders et al., 2015).

2.2. Test particle simulation

Using the steady state electric and magnetic fields calculated above we perform a test particle simulation, computing the trajectories by integrating the Lorentz force using Boris' CYLRAD algorithm (e.g., Hockney and Eastwood, 1988). Test particles, representing either ions or nano dust, are emitted on spherical shells centred on the nucleus, which is treated as an obstacle with a radius of 5 km. For each run presented in Sections. 3 and 4, one million trajectories were calculated. For each time step the test particle's contribution to the local density is saved on a grid in configuration space. The thus saved values are used to plot the density as a function of the spatial coordinates as shown in Fig. 2a and e. The contribution of each test particle to the velocity distribution functions is saved for predefined spherical probes, shown by red circles in Fig. 2a and e, if the particle passes through the sphere. The difference between panels a-d and panels e-h lies in that the size of the source is smaller in the former than in the latter set of panels.

Fortran source code for the test particle simulation program has been deposited with this article as supplementary material.

3. Cometary ion distributions

At comet Halley a radial gas velocity component of about 1 km/s was observed (Coates et al., 1989). Nilsson et al. (2015a) reported a velocity of 400 m/s as the Rosetta spacecraft was approaching comet 67P/Churyumov-Gerasimenko in 2014. We use a value of 700 m/s, as measured by the VIRTIS instrument on Rosetta in August 2014 (Gulkis et al., 2015).

In order to study the effects of contributions by ion sources of different sizes we have run the test particle simulation for water ions (H_2O^+) emitted from a spherical shell with a radius of 150 km and for one whose radius is 750 km.

Table 2: Hybrid model parameters at 1.45 AU. n_p^{sw} is the solar wind proton density, U^{sw} the solar wind velocity, T_e and T_p the electron and proton temperatures, and **B** the solar wind magnetic field vector. $Q(\mathrm{H_2O^+})$ is the production rate of $\mathrm{H_2O^+}$ ions, arising from the photoionisation of the cometary neutral $\mathrm{H_2O}$. Only ionisation within the simulation volume is included, explaining the difference between this value and the neutral production rate in Table 1. Finally, $k_{h\nu}$ is the photoionisation rate at 1.45 AU for low solar activity from Huebner et al. (1992).

n_p^{sw} [cm^{-3}]	n_α^{sw}	U^{sw} [km s^{-1}]	$(B_x, B_y, B_z)_{\mathrm{sw}}$ [nT]	T_{p} [K]	$Q(\mathrm{H_2O^+})$ [s^{-1}]	$k_{h\nu}$ [s^{-1}]
4.82	$0.04 \times n_p^{\mathrm{sw}}$	400	$(0, 4.39, 0)$	10^5	1.60×10^{25}	1.57×10^{-7}

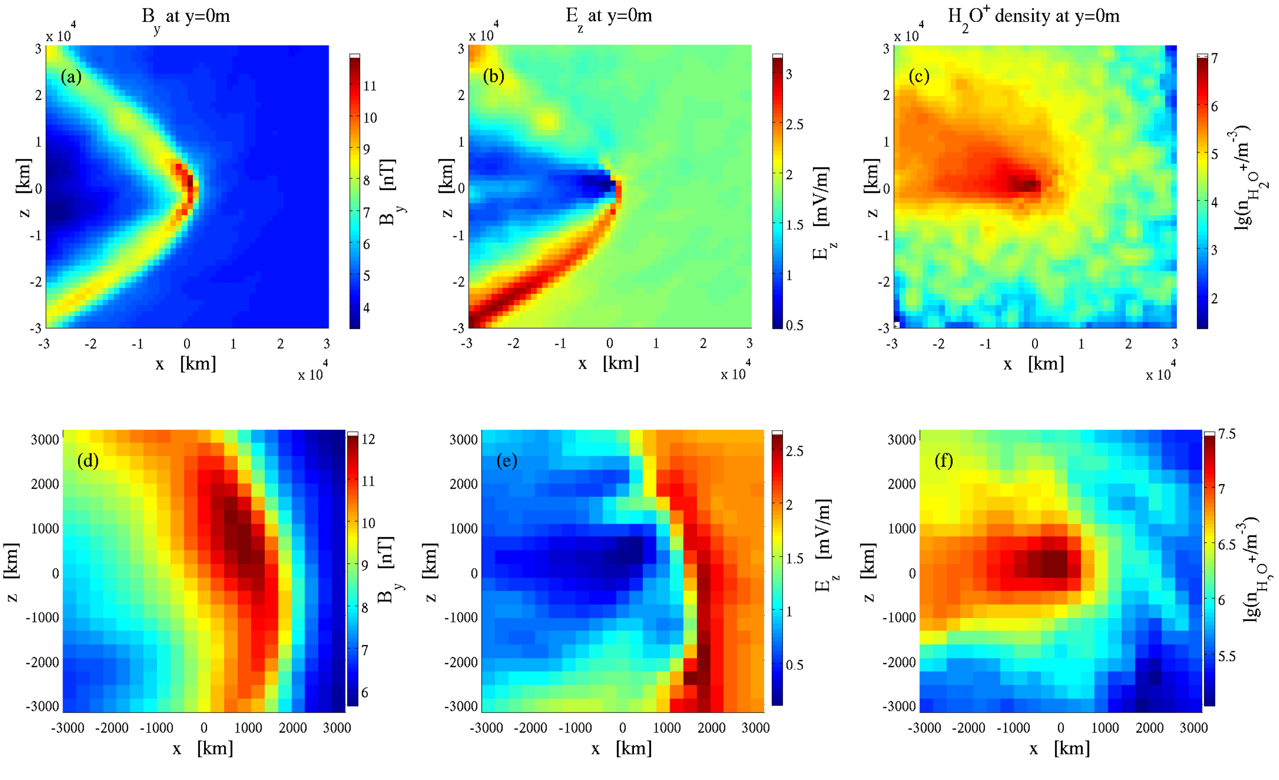

Figure 1: Hybrid model simulation results in the x–z plane ($y = 0$). The magnetic field vector points into the plane, while the solar wind velocity points in the $-x$ direction. (a) B_y. (b) E_z. (c) $\mathrm{H_2O^+}$ density. The bottom panels displays closeups of the quantities shown in the top panels: (d) B_y, (e) E_z, and (f) $\mathrm{H_2O^+}$ density.

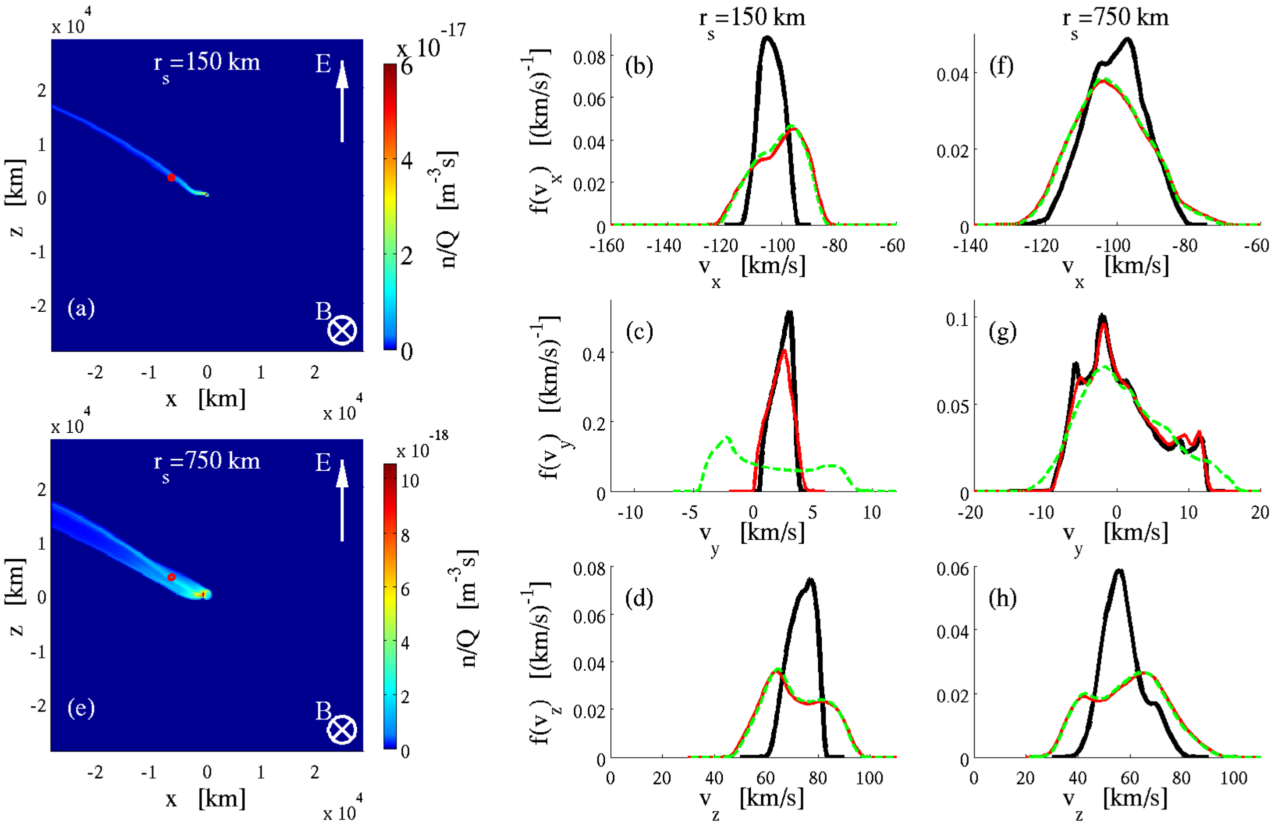

Figure 2: Water ion densities and distribution functions. (a) H_2O^+ ion density in the x–z plane ($y = 0$), normalised to the H_2O^+ production rate of a spherical source with radius 150 km. (b) Distribution function $f(v_x)$ for H_2O^+ ions at the position of the circle shown in panel (a). Panel (c) shows $f(v_y)$ and panel (d) $f(v_z)$ at that same position. Panel (e) shows the H_2O^+ ion density in the x–z plane ($y = 0$), normalised to the H_2O^+ production rate of a spherical source with radius 750 km and panels (f-h) show the distribution functions $f(v_x)$, $f(v_y)$, and $f(v_z)$ for the 750 km radius source. The black curves show the equilibrium distributions, the red curves show distributions affected by fluctuations in **E** that are perpendicular to **B**, and for the green curves the angle between the fluctuation electric field and **B** is 80°.

The hybrid simulation does itself contain water ions that, in principle, could be used for this purpose. However, the number of particles in a test particle simulation can be made much larger, yielding better statistics for the distribution function. The source distribution is a Maxwellian with a bulk velocity of 700 m/s directed radially outward, and a thermal speed $v_{\rm th} = \sqrt{2k_{\rm B}T_{\rm i}/m_{\rm i}} = 500\,{\rm m/s}$, which is within the temperature range observed at comet Halley (Lämmerzahl et al., 1987). The water ion density in the x–z plane ($y = 0$) is shown in Fig. 2a and e respectively. The colour scale is linear and the density has been normalised to the water ion production rate. In the smaller source case that is shown in Fig. 2a, the ions form a distinct beam, which is the beginning of a cycloid trajectory that would continue downstream had the simulation box extended farther in that direction. The red circle shows the position for which distribution functions are shown in Fig. 2b-d. It is seen from Fig. 2e that the larger source gives rise to a disproportionally wider beam, as the radius of curvature of the ion trajectories is different on the two sides of it. A beam within the beam extends from the region around the intersection of the source sphere and the negative x axis; it passes the red circle and continues over to the high z side of the beam. The difference between the two cases is that the 750 km radius source is large enough that ions emitted from different parts of it experience different fields, whereas particles emitted from the smaller source move through fields that are nearly equal.

The distribution functions for the ions at the position of the red circles are shown in Fig. 2b-d for the source with a radius of 150 km and in Fig. 2f-h for the 750 km radius source. In both cases the circle is at the position $(x, y, z) = (-6.6, 0, 3.3) \times 10^6\,{\rm m}$. The distribution function is computed from all test particles passing through a sphere of radius 500 km with its centre at that position. The equilibrium distributions – that is to say, those without fluctuations – are shown by the thick black lines, and two different cases where electric field fluctuations were added are shown by the red and green lines. Some of these lines overlap. We consider first the equilibrium distributions. The presence of two populations at the position of the circle in Fig. 2e, where the narrow beam traverses the wide beam, is seen also by the broader distribution in Fig. 2f, containing two peaks in the v_x component, a main peak at $-90\,{\rm km\,s^{-1}}$ and a secondary one at $-110\,{\rm km\,s^{-1}}$. As the fields $\mathrm{E}(x, y, z)$ and $\mathrm{B}(x, y, z)$ are the same in both cases and the particle trajectories depend only on these fields and the boundary conditions, we conclude that distributions with distinctly different shapes are possible even in the absence of plasma waves or other scattering processes. Instead the difference in shape is a result of the different sizes of the cometary ion sources.

The widening of the distribution in the v_y direction and its double-peaked nature is due to the y component of the electric field being directed in toward the $y = 0$ plane. This effect is seen in both Figs. 2c and g, but is much larger for the larger source. The larger source exhibits a complex v_y structure with multiple peaks throughout the velocity range. This indicates that different particles originating from different locations produce individual peaks in the velocity distribution and contribute to its overall widening in the y direction. In all six panels showing distribution functions it is seen that the distributions are wider than the thermal speed of the initial distribution, which was 500 m/s. As in the larger source, the smaller source's observed distribution, though significantly more collimated and showing less dispersion than for that of the larger source, is a result of ions arriving along slightly different trajectories and having experienced different fields during their transit.

As ions are emitted in all directions, some of them are emitted in the negative z direction. These will be slowed down to zero velocity before they are reflected back by the electric field toward positive z. Thus, there is a small region on the negative z side of the nucleus where the bulk velocity is close to zero. Only a small fraction of the reflected ions will be absorbed by the nucleus, it being much smaller than the source, and the energy of the reflected particles will remain the same as that of those emitted in the opposite direction, the force from the electric field being conservative. Thus, this should not substantially influence the distributions at the positions of observation in Fig. 2. However, as the electric field is inhomogeneous, the fact that the reflected ions have travelled along paths that are different from those of the ions injected in the positive z direction may contribute to the velocity dispersion.

Both sources considered here are small in comparison to the distance between the nucleus and the point where the distribution functions are observed. We therefore only see the contribution from ions generated close to the nucleus. The population of slower ions that were observed by Nilsson et al. (2015a,b) and that had been generated by ionisation near the spacecraft is not part of this study.

Oscillations of the electron flux in the millihertz range were observed at Mars (Winningham et al., 2006). Later oscillations of both electron and ion densities and ion velocities were observed near that planet (Gunell et al., 2008). Using magnetic field observations, Richter et al. (2015) reported fluctuations in a range from 1 to 100 mHz at comet 67P/Churyumov-Gerasimenko. They observed power spectral densities between 3 and $20\,{\rm nT^2Hz^{-1}}$ in the frequency range $1\,{\rm mHz} \leq f \lesssim 40\,{\rm mHz}$, and which fell off rapidly with frequency above 40 mHz. In order to obtain an estimate of the extent to which electric field fluctuations affect the distribution functions, we have performed two test particle simulations with a prescribed time-dependent electric field added to the equilibrium field. In the first run the fluctuation electric field $\mathbf{E}_1$ is exactly perpendicular to $\mathbf{B}$ (red curves in Fig. 2), and in the second run the angle between $\mathbf{E}_1$ and $\mathbf{B}$ is 80 degrees (green curves), which means that there is a small parallel component. The field is computed in the following way:

$$\mathbf{E}_1 = \mathbf{E}_a \cos\left(\pi \frac{r - (r_\mathrm{o} + r_\mathrm{i})/2}{(r_\mathrm{o} - r_\mathrm{i})}\right) \sin(2\pi f t + \phi), \qquad (2)$$

where r is the distance to the centre of the comet, $r_\mathrm{i} = 1.5 \times 10^6$ m is the inner radius of the fluctuation region, and $r_\mathrm{o} = 2 \times 10^7$ m is its outer radius. The fluctuation frequency is $f = 5$ mHz, and ϕ is the phase of the fluctuation, which is chosen at random at $t = 0$ for each test particle. The 5 mHz frequency is in the millihertz range, where oscillations could be expected. At this frequency oscillation period is 200 s, which is on the same order of magnitude as the approximately 100 s it takes an ion to move through the fluctuation region. In Eq. (2) the vector $\mathbf{E}_a$ represents the peak amplitude of the fluctuations:

$$\mathbf{E}_a = \frac{\hat{E}_1}{\sqrt{2}} \left[\mathbf{u}_B \left(\mathbf{u}_B \cdot (\mathbf{u}_y + \mathbf{u}_z)\right) \sin(\alpha) + \right.$$
$$\left. (\mathbf{u}_y + \mathbf{u}_z - \mathbf{u}_B \left(\mathbf{u}_B \cdot (\mathbf{u}_y + \mathbf{u}_z)\right)) \cos(\alpha)\right], \qquad (3)$$

where $\mathbf{u}_y$, $\mathbf{u}_z$, and $\mathbf{u}_B$ are unit vectors in the y, z, and $\mathbf{B}$ directions respectively. The angle between the perpendicular direction and $\mathbf{E}_a$ is $\alpha = 0$ in the perpendicular case and $\alpha = 10°$ in the case with a small parallel component. In order to study low amplitude fluctuations we have chosen a peak fluctuation amplitude of $\hat{E}_1 = 0.2$ mV/m, which is about an order of magnitude below the solar wind electric field. Since the magnetic field is predominantly in the y direction, this means that the electric field direction is close to parallel to the z axis, and that the magnetic field aligned component, in the case there is one, is approximately in the y direction.

The fluctuation field described by Eqs. (2) and (3) is not self-consistent and its spatial dependence has been chosen to ensure that all ions pass the fluctuation region, in order to see how the fluctuations influence the distribution function. The distribution functions are widened by the fluctuations. Comparing Fig. 2b and d, it is seen that the widening of the v_z component is larger than that of the v_x component. This is a result of the fluctuating electric field pointing in the z direction and therefore affecting the v_z component directly. However, the distribution in the v_x dimension is also affected by the fluctuations, as the velocity vectors of the particles are rotated by the magnetic field. For the larger source the same tendency is seen in Fig. 2f and h. The widening of the distributions due to fluctuations is relatively less significant there, because the equilibrium distributions were already wider in the case of the large than in that of the small source.

In the y direction there is a significant fluctuation field only in the case when there is a component parallel to the magnetic field as shown by the green dashed lines in Figs. 2c and g. The widening of the distribution in Fig. 2c is of the order of the width of the unperturbed distribution, and as ions are accelerated in either the positive or negative y direction fewer are left at low v_y values, causing the distribution to be double peaked. For the larger source the fluctuations merely smooth out the large peaks that form in the equilibrium v_y distribution.

The v_z distributions have become double peaked under the influence of fluctuations, although such a tendency could be descried also for the equilibrium distributions. For the already much broader distributions of the large source (Fig. 2f-h) thick tails develop in all directions.

4. Acceleration of nano dust

In this section, we report results from simulation of dust particles with radii in the 1–10 nm range. This nano dust is smaller than typical wavelengths of sunlight, and the effect of the photon pressure on their motion is therefore neglected.

Dust grains that are leaving the cometary nucleus will be accelerated by the outward gas flow. As the distance from the nucleus increases the force on the dust grains will diminish with the decreasing gas density. The source of the dust in the test particle simulation is a spherical shell of radius 150 km, assuming that the drag force from the gas on the dust is negligible at this distance. In Fig. 3a-c we compare dust trajectories for three different initial velocities, 50, 300, and 700 m/s. Following Czechowski and Mann (2010) we assume a charge-to-mass ratio of $q/m = 10^3$ C/kg for 10 nm dust and that the dust grains are spheres composed of material with mass density $\rho = 2500\,\mathrm{kg\,m^{-3}}$. This means that a dust grain with radius $r_d = 10$ nm has a mass of $m = 1.05 \times 10^{-20}$ kg and that its charge is $q = 65e$.

As an estimate of the time scale for charging a dust grain to that charge we assume a constant photoemission current I_e and calculate the charging time $T_\mathrm{c} = q/I_\mathrm{e}$. Feuerbacher et al. (1972) found a photoemission current density of $J_\mathrm{e} = 4.5\,\mu\mathrm{Am^{-2}}$ at a photoelectric yield of 0.07 in samples of dust taken from the moon. Gail and Sedlmayr (1980) found that for grains with diameters below 0.1 μm the photoelectric yield is 1.0. The grains considered here are all smaller than 0.1 μm, so we scale the photoemission current density by the yield and by the square of the heliocentric distance to obtain $J_\mathrm{e} = 4.5\,\mu\mathrm{Am^{-2}}/(0.07 \times 1.45^2) \approx 31\,\mu\mathrm{Am^{-2}}$. For a $r_d = 10$ nm grain to charge to $q = 65e$ we then have $T_\mathrm{c} = q/(\pi r_\mathrm{d}^2 J_\mathrm{e}) \approx 1.1 \times 10^3$ s. This is significantly less than transit time, $T = 8390$ s, for the dust grain to leave the system shown in Table 3. We therefore conclude that $q = 65e$ is an attainable value. In addition to solar radiation and plasma conditions the grain charge may also depend on grain properties, which we do not model.

Our calculations show that the outgoing dust beam becomes wider for higher initial speeds. However, also for an initial radial velocity component of 700 m/s (Fig. 3c) the dust grains move predominantly in the direction of $\mathbf{E}$, and on spatial scales on the order of 10^4 km it is the force from the electric field that is most important in determining the trajectory.

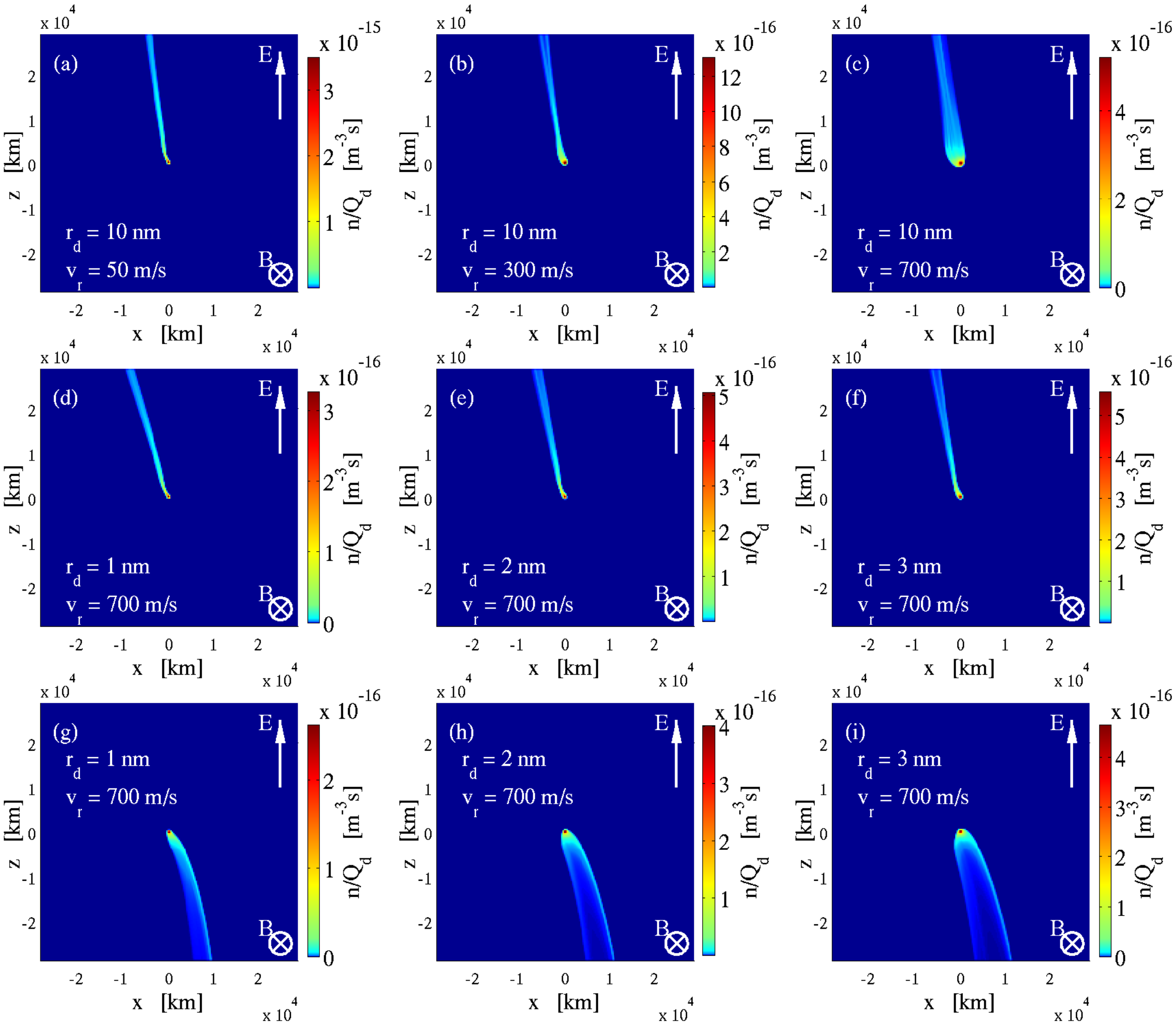

Figure 3: Dust densities, in the x–z plane ($y = 0$), for different initial speeds and different dust grain sizes. In panels (a), (b), and (c) the dust grain radius is 10 nm, and the initial radial velocity component is 50, 300, and 700 m/s respectively. In panels (d), (e), and (f) the radial velocity component is 700 m/s, and the dust grain radius is 1, 2, and 3 nm respectively. Panels (g), (h), and (i) show examples of negatively charged dust grains of radius 1, 2, and 3 nm and charge $-4e$, $-7e$, and $-11e$ respectively.

Table 3: Charge q, transit time T, and final speed v_f for dust particles with different radii and surface potentials. The transit times and final speeds were measured at the edge of the simulation box, 2.9×10^4 km from the nucleus. The source radius was $r_\mathrm{s} = 150$ km, and the initial radial bulk velocity component was $v_r = 700$ m/s.

	$V_\mathrm{d} \approx 5.4$ V	$V_\mathrm{d} \approx 9.4$ V	$V_\mathrm{d} \approx 13.4$ V
1 nm	$q = 4e$ $T = 1223$ s $v_\mathrm{f} = 74$ km/s	$q = 7e$ $T = 938$ s $v_\mathrm{f} = 98$ km/s	$q = 9e$ $T = 834$ s $v_\mathrm{f} = 111$ km/s
2 nm	$q = 7e$ $T = 2536$ s $v_\mathrm{f} = 35$ km/s	$q = 13e$ $T = 1884$ s $v_\mathrm{f} = 48$ km/s	$q = 19e$ $T = 1570$ s $v_\mathrm{f} = 57$ km/s
3 nm	$q = 11e$ $T = 3648$ s $v_\mathrm{f} = 24$ km/s	$q = 19e$ $T = 2814$ s $v_\mathrm{f} = 31$ km/s	$q = 28e$ $T = 2338$ s $v_\mathrm{f} = 38$ km/s
10 nm	$q = 37e$ $T = 10737$ s $v_\mathrm{f} = 7.4$ km/s	$q = 65e$ $T = 8390$ s $v_\mathrm{f} = 9.7$ km/s	$q = 93e$ $T = 7171$ s $v_\mathrm{f} = 12$ km/s

At a comet, there are dust grains of different sizes. In order to see how their respective sizes influence the acceleration we have computed trajectories for dust grains with radii $r_d = 1, 2, 3,$ and 10 nm. We assume that the grains in the size distribution, in an equilibrium state, are charged to the same surface potential (Kimura and Mann, 1998). We use this approach bearing in mind that the charging conditions can vary in the environment of the comet, but nonetheless a small positive charge is likely (Mann et al., 2014). We first find the potential of a dust grain with radius $r_d = 10$ nm, and then we use that potential to compute the charge of the smaller grains, rounding its value toward the nearest integral number of elementary charges. Using the simplification that the grain is spherical we obtain the potential

$$V_\mathrm{d}(r_\mathrm{d}) = \frac{q}{4\pi\epsilon_0 r_\mathrm{d}}. \quad (4)$$

The mass of a homogeneous sphere being $m = \rho 4\pi r_\mathrm{d}^3/3$ we have a charge-to-mass ratio:

$$\frac{q}{m} = \frac{3\epsilon_0}{\rho} V_\mathrm{d} \frac{1}{r_\mathrm{d}^2}. \quad (5)$$

For a 10 nm dust grain with $q/m = 10^3$ C/kg it follows from Eq. (5), with $\rho = 2500\,\mathrm{kg\,m^{-3}}$ as above, that the potential of the dust grain surface is $V_\mathrm{d} = 9.4$ V. This value is in the middle of the range of 4-14 V that has been computed for silicate grains at 1 AU (Mukai, 1981). The cases with different radii for the equilibrium dust grain charge, $V_\mathrm{d} = 9.4$ V, are summarised in the middle column of Table 3. For each case one million test particle trajectories were calculated; the source radius was $r_\mathrm{s} = 150$ km, and the initial radial bulk velocity component was $v_r = 700$ m/s, that is to say, we assume that the nano dust has been dragged along completely with the gas flow. It was seen in Fig. 3a-c that the value of v_r does not significantly change the dust grain trajectories. Dust densities normalised to the dust production rate are shown in Fig. 3d, e, f, and c for $r_\mathrm{d} = 1, 2, 3,$ and 10 nm respectively. The larger, more massive, grains are able to move farther radially before they are accelerated appreciably in the electric field direction, and they therefore form beams with larger angular spread than the small grains do. For example the width of the beam of the smallest grains in Fig. 3d is almost the same at the edge of the system as at its source.

We have used $V_\mathrm{d} = 9.4$ V even for the smallest particles of $r_\mathrm{d} = 1$ nm in Fig. 3d in order to illustrate the size dependence separately. However, it should be noted that 1 nm particles are unlikely to survive at potentials above 5 V as the electric field at the surface then reaches the threshold for Coulomb explosion, which is approximately 5×10^9 V/m (Mijoule et al., 2006).

Comparing the trajectories of the positively charged dust grains in Fig. 3a-f to the ion trajectories in Fig. 2 it is seen that the ions move along cycloid trajectories, of which only the beginning is seen in the figure, whereas the dust grains move along more or less straight lines. As the dust moves out of our simulation region and into the unperturbed solar wind also their paths will become cycloids, although their gyroradii will be much larger than those of the ions. In Fig. 3a-f, particularly in Fig. 3a where the grains have the lowest initial velocity, the trajectory is seen to curve slightly in the direction opposite to that of a cycloid. This is due to the non-uniform electric field, which is shown in Fig. 1b. The dust grains leave the source in the lower field region (blue in Fig. 1b), then they enter a region where E_z is stronger, and that causes them to be accelerated more rapidly in the positive z direction. The $\mathrm{H_2O^+}$ ions in Fig. 2a, on the other hand, stay in the lower field region throughout their journey, due to their smaller gyroradius.

The time T it takes a typical dust grain to leave the system is 938 s for the 1 nm dust and 8390 s for the 10 nm dust as is seen in Table 3. The test particle simulations are performed under the assumption of a steady state, which means that for the pictures shown in Fig. 3 to be true, the solar wind conditions must remain the same over one transit time. As it is more likely that these conditions are unchanged over a shorter period than a longer one, Fig. 3d is more likely to be an accurate description of the 1 nm dust density distribution than Fig. 3c is for the 10 nm dust.

Charging of the nano dust is a stochastic process, and in the comet environment, not all dust grain will be charged to the equilibrium potential. Photo-emission of electrons caused by ultraviolet photons from the sun contribute to a positive dust grain charge. On the other hand, the dust can collect electrons from the surrounding plasma, and this process serves to decrease the charge of positively charged grains. In order to see the effect of a variation of the dust grain charge we have computed trajectories for different dust grain potentials. In Table 3 we have included simulation results for $V_\mathrm{d} = 5.4$ V and 13.4 V – that is to say – four volts above and below the equilibrium value. As expected the final speed increases and the transit time decreases with the dust grain potential.

The gyroradius for the dust grains is much larger than the simulation box, and their motion inside that box can be approximated by that of a charged particle in a constant electric field. Thus, assuming that E is a constant, $B = 0$, and $v(t = 0) = 0$, the speed v_f after a fixed distance a is

$$v_\mathrm{f} = \sqrt{2aE}\cdot\sqrt{\frac{q}{m}} \tag{6}$$

The final speed v_f for a dust grain leaving the system is shown as a function of $\sqrt{q/m}$, in Fig. 4a for all dust grains in Table 3. The final speed is proportional to $\sqrt{q/m}$, confirming the validity of the approximation. The constant of proportionality in Eq. (6) can be determined from the slope of the black line in Fig. 4a, and we have $\sqrt{2aE} = 300\,\mathrm{V}^{1/2}$. With $a = 2.9 \times 10^4\,\mathrm{km}$, the distance from the comet nucleus to the edge of the simulation box which may serve as an order of magnitude estimate of the size of the coma, this corresponds to an electric field $E \approx 1.5\,\mathrm{mV/m}$, which is within the range of fields that the particle goes through as seen in Fig. 1b. Combining Eqs. (5) and (6) we obtain v_f as a function of r_d and V_d.

$$v_\mathrm{f} = \sqrt{2aE}\cdot\sqrt{\frac{3\epsilon_0}{\rho}V_\mathrm{d}}\cdot\frac{1}{r_\mathrm{d}} \tag{7}$$

Fig. 4b shows the final speed as a function of $1/r_\mathrm{d}$ for all dust grains in Table 3. The black line is given by Eq. (7) for the equilibrium potential. The grains that are charged to $V_\mathrm{d} = 9.4\,\mathrm{V}$ agree well with the line, and for the others proportionality still applies for their respective potentials according to Eq. (7). Fig. 4c shows the final speed as a function of r_d for five different potentials centred on the equilibrium potential. For $V_\mathrm{d} = 9.4\,\mathrm{V}$ dust grains that are 10 nm or smaller reach 10 km/s before leaving the system. For $V_\mathrm{d} = 13.4\,\mathrm{V}$ and 17.4 V grains with radii 11 nm and 13 nm respectively will reach that speed.

Dust grains may become negatively charged by picking up electrons from the dense plasma close to the nucleus. Figs. 3g-i show dust densities in the $x - z$ plane for negatively charge dust grains of radius 1, 2, and 3 nm. The charge on each grain is $q = -4e$, $-7e$, and $-11e$ in the three panels respectively. This corresponds to a potential $V_\mathrm{d} = -5.4\,\mathrm{V}$. We have used the lower potential, because the charging process rapidly becomes less efficient as the plasma density decreases with the distance to the nucleus. The dust grains have a positive v_x component due to the negative E_x component close to the nucleus. As the grains leave the system this v_x decreases and we see the beginning of a cycloid orbit as expected. The E_x component can be seen by the electric field lines shown in Fig. 5. The difference in shape and width between the bottom and the middle rows of Fig. 3 is caused by the asymmetry in the electric field direction seen in Fig. 5. In the case of negatively charged grains the beam is wider, because grains

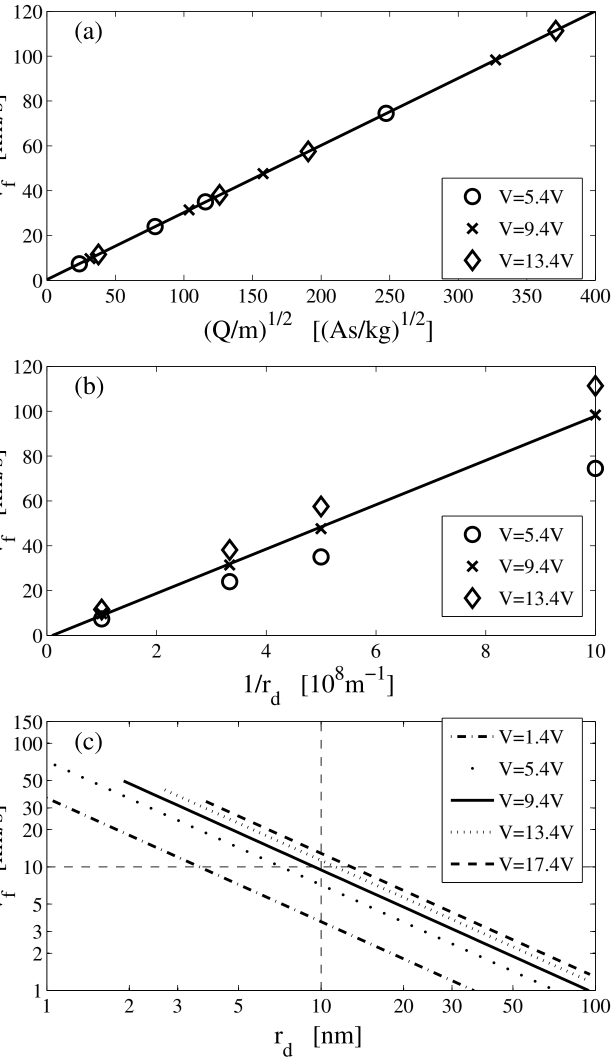

Figure 4: (a) Final speed v_f for dust grains leaving the system as a function of the square root of the charge to mass ratio. The black line is a least squares fit to the points shown. (b) v_f as a function of $1/r_\mathrm{d}$. The black line is given by Eq. (7) for $V_\mathrm{d} = 9.4\,\mathrm{V}$. (c) v_f as a function of $1/r_\mathrm{d}$ for different dust grain potentials. The curves are shown for radii corresponding to electric fields below $5 \times 10^9\,\mathrm{V/m}$ to avoid the Coulomb explosion regime.

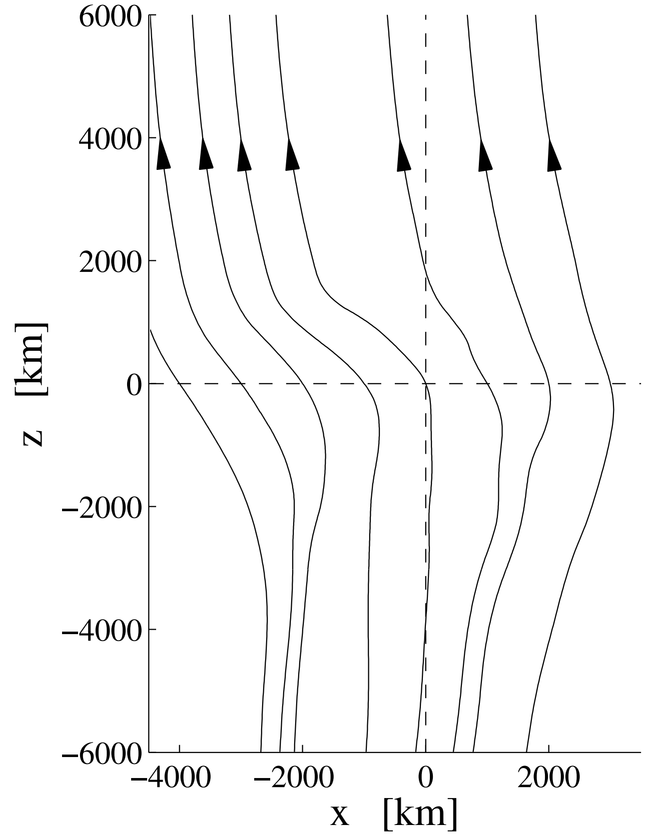

Figure 5: Lines showing the direction of the electric field in the x–z plane near the origin.

emitted towards positive z spend time in a stronger negative E_x field than those that moved in the negative z direction from the start. In the case of positively charged grains, all grains pass through the strong negative E_x region, and those that first turn around at $z < 0$ receive a relatively small additional acceleration by the negative E_x component.

5. Discussion

We have performed test particle simulations of cometary water ions and charged dust grains in electric and magnetic fields that were computed using a quasi-neutral hybrid model of the solar wind interacting with a comet. The cometary parameters were chosen to reflect the predicted state of comet 67P/Churyumov-Gerasimenko when it is at 1.45 AU heliocentric distance.

The velocity distribution function for the ions at their source was modelled by a drifting Maxwellian with a thermal speed of 500 m/s and a bulk velocity of 700 m/s directed radially outward, which is what would be expected for a neutral gas flowing outward from the nucleus of the comet. The newly ionised population initially maintains the distribution function of the neutrals. The distribution is probed at a distance on the order of 10^4 km from the nucleus (Fig. 2a), and there the distribution function is widened significantly in all directions, but more in the x and z directions, in which the ions have been accelerated. The ions arrive at the probe along different paths and have therefore undergone different amounts of acceleration. Ions reach different velocities at the probe position in part due to the non-uniformity of the field, which lets different ions pass through regions of different fields, but also as a result of their initial velocities being directed differently with respect to these fields. The resulting distribution function is a superposition of the contributions from these different ions having different velocities, and this leads to distributions that are quite different from the initial distributions. The effect of the different initial ion velocity direction is the same for both the 150 km radius source, and that which is five times larger. The non-uniformity of the fields becomes more important for the larger source, for which multiple-peak distributions are seen in Figs. 2f and g.

Fluctuations imposed on the ions in the form of an oscillating electric field of 0.2 mV/m peak amplitude at a frequency of 5 mHz resulted in a further broadening of the distributions in the direction in which this field was applied. In the case of electric field fluctuations in the direction parallel to the magnetic field, mostly in the y direction, the sharp peaks in the distribution were made smoother. The fluctuations modelled here are in the amplitude of the electric field. If instead the direction of the field were to fluctuate, a similar effect would be expected, as an oscillating electric field would be imposed in a direction where the equilibrium state has no electric field. The distance between the nucleus and the position where we probed the distribution function was smaller than the H_2O^+ gyroradius. To scatter the ions into shell-like distributions such as those observed by Coates et al. (1989) one would need much larger distances. The non-Maxwellian distribution functions that are seen in these simulations may have implications for the nature of the wave modes that occur in the plasma on ion acoustic scales (Gunell and Skiff, 2001).

We have computed trajectories of charged dust emitted from the cometary nucleus. Dust grains are expected to become positively charged by photo-emission of electrons due to ultraviolet radiation from the sun. In a plasma a competing process is the collecting of electrons from the plasma. The latter process is expected to be more efficient in the denser plasma close to the comet's nucleus. As the dust grains move away from the nucleus, photo-emission becomes the dominating process. Both photo-emission and the absorption of electrons are stochastic processes, and in the cometary environment one would expect a distribution of different charges. For positively charged dust, we have calculated trajectories for different charges to shed light on the effect of dust charging. There is no fundamental difference between the trajectories for these differently charged grains, only the expected effect that a higher charge leads to higher acceleration is seen. Thus, with a distribution of differently charged dust, one would also expect a distribution of different dust velocities. Dust can become negatively charged in the dense plasma close to the nucleus, and it would then move along trajectories toward negative values of z, as shown in Fig. 3. As the process of collecting electrons from the plasma decreases in efficiency when the dust grain moves away from the nucleus, photo-emission may first neutralise it and then charge it positively. Changing the sign of the charge would change the trajectory completely and scatter dust over large parts of the coma.

The dust grains considered here have radii between 1 and 10 nm, and being smaller than the wavelength of most of the solar radiation they are less subjected to the radiation pressure that is dominating for larger dust. Depending on dust size and neutral gas density and speed, the dust grains may be accelerated to different radial speeds by means of drag forces close to the nucleus. We do not model the drag force, which is important only the first few kilometres from the nucleus, but instead use different initial bulk speeds to study its effect on the dust motion. We see in Fig. 3a-c that the dust beam is noticeably widened for the largest radial initial velocity component of 700 m/s, but that it is the acceleration by the electric field which is the dominating influence on the trajectory in all three cases. Our test particle simulations are carried out for charge to mass ratios ranging from 6×10^2 C/kg to 1.4×10^5 C/kg. The dust sizes we discuss are subject to the uncertainties in estimating the surface charge of nano dust. The quantity that defines the trajectories of charged particles is their charge to mass ratio. We have computed trajectories for dust grains with different radii, assuming the same mass density ρ of the material of which the grains are made. For dust with different mass densities, the same trajectories would be obtained for a different set of radii determined by Eq. (5).

While dust of all sizes is accelerated more or less straight out of the cometary environment in the direction of the electric field as is seen in Fig. 3, the time it takes for this to happen varies with dust grain size. The smallest grains studied here ($r_\mathrm{d} = 1\,\mathrm{nm}$) leave the system in about ten minutes, whereas for the largest grains ($r_\mathrm{d} = 10\,\mathrm{nm}$) this takes close to two hours, and for grains larger than that it would take even longer. If the solar wind magnetic field direction changes during the transit of a dust particle it will be deflected and accelerated in a new direction, and dust grains may be found in a larger region of the comet rather than in a distinct beam. As the transit times for small dust are rather short these are the most likely to be in distinct beams, and large dust grains may stay in the comet environment for longer periods being accelerated in different directions following the changes in the solar wind magnetic field.

For the purpose of finding the speed of the dust grain at a fixed distance from the nucleus, their acceleration can be approximated by a simple model of a constant electric field. In this way we can compute the speed the dust will reach before they leave the system as a function of their radius. It is seen in Fig. 4c that dust with $r_\mathrm{d} \lesssim 10\,\mathrm{nm}$ can reach speeds above 10 km/s. Since large grains move more slowly than small grains also the relative velocity can become large, leading to fragmentation of the larger dust grains, although given the uncertainties of the densities of both the small and large dust populations we cannot compute the probability of collisions between them. Another possibility is the impact of nano dust on very large grains, such as the objects with diameters in the 0.14–0.50 m range observed by the OSIRIS camera onboard Rosetta (Davidsson et al., 2015), leading to sputtering of the material of these objects. Fragmentation and sputtering may in turn create a secondary source of small dust distributed along the path of the primary nano dust.

Acknowledgment

This work was supported by the Belgian Science Policy Office through the Solar-Terrestrial Centre of Excellence and by PRODEX/ROSETTA/ROSINA PEA 4000107705. C.S.W., M.A. and E.K. acknowledge the support of the Academy of Finland (project No. 251573).

References

Chandrasekar, S., 1961. Hydrodynamic and Hydromagnetic Stability. Clarendon, Oxford. chapter 11.

Clark, B.C., Green, S.F., Economou, T.E., Sandford, S.A., Zolensky, M.E., McBride, N., Brownlee, D.E., 2004. Release and fragmentation of aggregates to produce heterogeneous, lumpy coma streams. J. Geophys. Res. (Planets) 109, E12S03. doi:`10.1029/2004JE002319`.

Coates, A.J., Johnstone, A.D., Huddleston, D.E., Wilken, B., Jockers, K., Borg, H., Amata, E., Formisano, V., Bavassano-Cattaneo, M.B., Winningham, J.D., Gurgiolo, C., Neubauer, F.M., 1993. Pickup water group ions at comet Grigg-Skjellerup. Geophys. Res. Lett. 20, 483–486. doi:10.1029/93GL00174.

Coates, A.J., Johnstone, A.D., Wilken, B., Jockers, K., Glassmeier, K.H., 1989. Velocity space diffusion of pickup ions from the water group at comet Halley. J. Geophys. Res. 94, 9983–9993. doi:10.1029/JA094iA08p09983.

Czechowski, A., Mann, I., 2010. Formation and acceleration of nano dust in the inner heliosphere. The Astrophysical Journal 714, 89–99. doi:10.1088/0004-637X/714/1/89.

Davidsson, B.J.R., Gutiérrez, P.J., Sierks, H., Barbieri, C., Lamy, P.L., Rodrigo, R., Koschny, D., Rickman, H., Keller, H.U., Agarwal, J., A'Hearn, M.F., Barucci, M.A., Bertaux, J.L., Bertini, I., Bodewits, D., Cremonese, G., Deppo, V.D., Debei, S., Cecco, M.D., Fornasier, S., Fulle, M., Groussin, O., Güttler, C., Hviid, S.F., Ip, W.H., Jorda, L., Knollenberg, J., Kovacs, G., Kramm, J.R., Kührt, E., Küppers, M., Forgia, F.L., Lara, L.M., Lazzarin, M., Lopez Moreno, J.J., Lowry, S., Magrin, S., Marzari, F., Michalik, H., Moissl-Fraund, R., Naletto, G., Oklay, N., Pajola, M., Snodgrass, C., Thomas, N., Tubiana, C., Vincent, J.B., 2015. Orbital elements of the material surrounding comet 67P/Churyumov-Gerasimenko. Astronomy & Astrophysics doi:10.1051/0004-6361/201525841.

Eddington, A.S., 1910. The envelopes of comet Morehouse (1908 c). Monthly Notices of the Royal Astronomical Society 70, 442–458.

Feuerbacher, B., Anderegg, M., Fitton, B., Laude, L.D., Willis, R.F., Grard, R.J.L., 1972. Photoemission from lunar surface fines and the lunar photoelectron sheath, in: Metzger, A.E., Trombka, J.I., Peterson, L.E., Reedy, R.C., Arnold, J.R. (Eds.), Lunar and Planetary Science Conference Proceedings, pp. 2655–2663.

Fulle, M., Colangeli, L., Agarwal, J., Aronica, A., Della Corte, V., Esposito, F., Grün, E., Ishiguro, M., Ligustri, R., Lopez Moreno, J.J., Mazzotta Epifani, E., Milani, G., Moreno, F., Palumbo, P., Rodríguez Gómez, J., Rotundi, A., 2010. Comet 67P/Churyumov-Gerasimenko: the GIADA dust environment model of the Rosetta mission target. Astronomy & Astrophysics 522, A63. doi:10.1051/0004-6361/201014928.

Gail, H.P., Sedlmayr, E., 1980. On the photoelectric yield of insulating dust grains. Astronomy & Astrophysics 86, 380–385.

Gronoff, G., Rahmati, A., Wedlund, C.S., Mertens, C.J., Cravens, T.E., Kallio, E., 2014. The precipitation of keV energetic oxygen ions at Mars and their effects during the comet Siding Spring approach. Geophys. Res. Lett. 41, 4844–4850. doi:10.1002/2014GL060902.

Gulkis, S., Allen, M., von Allmen, P., Beaudin, G., Biver, N., Bockelée-Morvan, D., Choukroun, M., Crovisier, J., Davidsson, B.J.R., Encrenaz, P., Encrenaz, T., Frerking, M., Hartogh, P., Hofstadter, M., Ip, W.H., Janssen, M., Jarchow, C., Keihm, S., Lee, S., Lellouch, E., Leyrat, C., Rezac, L., Schloerb, F.P., Spilker, T., 2015. Subsurface properties and early activity of comet 67P/Churyumov-Gerasimenko. Science 347, 709. doi:10.1126/science.aaa0709.

Gunell, H., Amerstorfer, U.V., Nilsson, H., Grima, C., Koepke, M., Fränz, M., Winningham, J.D., Frahm, R.A., Sauvaud, J.A., Fedorov, A., Erkaev, N.V., Biernat, H.K., Holmström, M., Lundin, R., Barabash, S., 2008. Shear driven waves in the induced magnetosphere of Mars. Plasma Physics and Controlled Fusion 50, 074018. doi:10.1088/0741-3335/50/7/074018.

Gunell, H., Skiff, F., 2001. Weakly damped acoustic-like ion waves in plasmas with non-Maxwellian ion distributions. Physics of Plasmas 8, 3550–3557. doi:10.1063/1.1386428.

Hansen, K.C., Bagdonat, T., Motschmann, U., Alexander, C., Combi, M.R., Cravens, T.E., Gombosi, T.I., Jia, Y.D., Robertson, I.P., 2007. The plasma environment of comet 67P/Churyumov-Gerasimenko throughout the Rosetta main mission. Space Science Reviews 128, 133–166. doi:10.1007/s11214-006-9142-6.

Haser, L., 1957. Distribution d'intensité dans la tête d'une comète. Bulletin de la Societe Royale des Sciences de Liege 43, 740–750.

Hockney, R.W., Eastwood, J.W., 1988. Computer Simulation Using Particles. IOP Publishing Ltd, Techno House, Redcliffe Way, Bristol BS1 6NX, England.

Hsu, H.W., Küger, H., Postberg, F., 2012. Dynamics, composition, and origin of jovian and saturnian dust-stream particles, in: Mann, I., Meyer-Vernet, N., Czechowski, A. (Eds.), Nanodust in the Solar System: Discoveries and Interpretations. Springer Berlin Heidelberg. volume 385 of *Astrophysics and Space Science Library*, pp. 77–117. doi:10.1007/978-3-642-27543-2_5.

Hsu, H.W., Postberg, F., Kempf, S., Trieloff, M., Burton, M., Roy, M., Moragas-Klostermeyer, G., Srama, R., 2011. Stream particles as the probe of the dust-plasma-magnetosphere interaction at saturn. J. Geophys. Res. (Space Physics) 116, 9215. doi:10.1029/2011JA016488.

Huebner, W.F., Keady, J.J., Lyon, S.P., 1992. Solar photo rates for planetary atmospheres and atmospheric pollutants. Astrophys. Space Sci. 195, 1–289. doi:10.1007/BF00644558.

Jarvinen, R., Alho, M., Kallio, E., Wurz, P., Barabash, S., Futaana, Y., 2014. On vertical electric fields at lunar magnetic anomalies. Geophys. Res. Lett. 41, 2243–2249. doi:10.1002/2014GL059788.

Kallio, E., 2005. Formation of the lunar wake in quasi-neutral hybrid model. Geophys. Res. Lett. 32, 6107. doi:10.1029/2004GL021989.

Kallio, E., Fedorov, A., Budnik, E., Säles, T., Janhunen, P., Schmidt, W., Koskinen, H., Riihelä, P., Barabash, S., Lundin, R., Holmström, M., Gunell, H., Brinkfeldt, K., Futaana, Y., Andersson, H., Yamauchi, M., Grigoriev, A., Sauvaud, J.A., Thocaven, J.J., Winningham, J.D., Frahm, R.A., Sharber, J.R., Scherrer, J.R., Coates, A.J., Linder, D.R., Kataria, D.O., Kozyra, J., Luhmann, J.G., Roelof, E., Williams, D., Livi, S., Curtis, C.C., Hsieh, K.C., Sandel, B.R., Grande, M., Carter, M., McKenna-Lawler, S., Orsini, S., Cerulli-Irelli, R., Maggi, M., Wurz, P., Bochsler, P., Krupp, N., Woch, J., Fränz, M., Asamura, K., Dierker, C., 2006. Ion escape at Mars: Comparison of a 3-D hybrid simulation with Mars Express IMA/ASPERA-3 measurements. Icarus 182, 350–359. doi:10.1016/j.icarus.2005.09.018.

Kallio, E., Janhunen, P., 2003. Modelling the solar wind interaction with Mercury by a quasi-neutral hybrid model. Annales Geophysicae 21, 2133–2145. doi:10.5194/angeo-21-2133-2003.

Kallio, E., Jarvinen, R., 2012. Kinetic effects on ion escape at Mars and Venus: Hybrid modeling studies. Earth, Planets, and Space 64, 157–163. doi:10.5047/eps.2011.08.014.

Kimura, H., Mann, I., 1998. The electric charging of interstellar dust in the solar system and consequences for its dynamics. The Astrophysical Journal 499, 454–462. doi:10.1086/305613.

Koenders, C., Glassmeier, K.H., Richter, I., Ranocha, H., Motschmann, U., 2015. Dynamical features and spatial structures of the plasma interaction region of 67P/Churyumov-Gerasimenko and the solar wind. Planetary and Space Science 105, 101–116. doi:10.1016/j.pss.2014.11.014.

Lämmerzahl, P., Krankowsky, D., Hodges, R.R., Stubbemann, U., Woweries, J., Herrwerth, I., Berthelier, J.J., Illiano, J.M., Eberhardt, P., Dolder, U., Shulte, W., Hoffman, J.H., 1987. Expansion velocity and temperatures of gas and ions measured in the coma of comet P/Halley. Astronomy & Astrophysics 187, 169–173.

Lindsay, B.G., Sieglaff, D.R., Smith, K.A., Stebbings, R.F., 1997. Charge transfer of 0.5-, 1.5-, and 5-kev protons with h_2o: Absolute differential and integral cross sections. Phys. Rev. A 55, 3945–3946. doi:10.1103/PhysRevA.55.3945.

Mann, I., Czechowski, A., 2012. Causes and consequences of the existence of nanodust in interplanetary space, in: Mann, I., Meyer-Vernet, N., Czechowski, A. (Eds.), Astrophysics and Space Science Library, p. 195. doi:10.1007/978-3-642-27543-2_10.

Mann, I., Czechowski, A., Kimura, H., Köhler, M., Minato, T., Yamamoto, T., 2006. Physical properties of the dust in the solar system and its interrelation with small bodies, in: Daniela, L., Sylvio Ferraz, M., Angel, F.J. (Eds.), Asteroids, Comets, Meteors, pp. 41–65. doi:10.1017/S1743921305006678.

Mann, I., Meyer-Vernet, N., Czechowski, A., 2014. Dust in the planetary system: Dust interactions in space plasmas of the solar system. Physics Reports 536, 1–39. doi:10.1016/j.physrep.2013.11.001.

McBride, J.B., Ott, E., Boris, J.P., Owens, J.H., 1972. Theory and simulation of turbulent heating by the modified two-stream instability. Physics of Fluids 15, 2367–2383.

Mijoule, V., Lewis, L.J., Meunier, M., 2006. Coulomb explosion induced by intense ultrashort laser pulses in two-dimensional clusters. Phys. Rev. A 73, 033203. doi:`10.1103/PhysRevA.73.033203`.

Mukai, T., 1981. On the charge distribution of interplanetary grains. Astronomy & Astrophysics 99, 1–6.

Nilsson, H., Stenberg Wieser, G., Behar, E., Simon Wedlund, C., Gunell, H., Yamauchi, M., Lundin, R., Barabash, S., Wieser, M., Carr, C., Cupido, E., Burch, J.L., Fedorov, A., Sauvaud, J.A., Koskinen, H., Kallio, E., Lebreton, J.P., Eriksson, A., Edberg, N., Goldstein, R., Henri, P., Koenders, C., Mokashi, P., Nemeth, Z., Richter, I., Szego, K., Volwerk, M., Vallat, C., , Rubin, M., 2015a. Birth of a comet magnetosphere: A spring of water ions. Science 347. doi:`10.1126/science.aaa0571`.

Nilsson, H., Stenberg Wieser, G., Behar, E., Simon Wedlund, C., Kallio, E., Gunell, H., Edberg, N., Eriksson, A.I., Yamauchi, M., Koenders, C., Wieser, M., Lundin, R., Barabash, S., Mandt, K., Burch, J.L., Goldstein, R., Mokashi, P., Carr, C., Cupido, E., Fox, P.T., Szego, K., Nemeth, Z., Fedorov, A., Sauvaud, J.A., Koskinen, H., Richter, I., Lebreton, J.P., Henri, P., Volwerk, M., Vallat, C., , Geiger, B., 2015b. Evolution of the ion environment of comet 67P/Churyumov-Gerasimenko observations between 3.6 and 2.0 AU. Astronomy & Astrophysics , in press doi:`10.1051/0004-6361/201526142`.

Raadu, M.A., 1978. The role of electrostatic instabilities in the critical ionization velocity mechanism. Astrophysics and Space Science 55, 125–138. doi:`10.1007/BF00642584`.

Richardson, I.G., Cowley, S.W.H., Hynds, R.J., Tranquille, C., Sanderson, T.R., Wenzel, K.P., 1987. Observations of energetic water-group ions at comet Giacobini-Zinner - implications for ion acceleration processes. Planetary and Space Science 35, 1323–1345. doi:`10.1016/0032-0633(87)90118-8`.

Richter, I., Koenders, C., Auster, H.U., Frühauff, D., Götz, C., Heinisch, P., Perschke, C., Motschmann, U., Stoll, B., Altwegg, K., Burch, J., Carr, C., Cupido, E., Eriksson, A., Henri, P., Goldstein, R., Lebreton, J.P., Mokashi, P., Nemeth, Z., Nilsson, H., Rubin, M., Szegö, K., Tsurutani, B.T., Vallat, C., Volwerk, M., Glassmeier, K.H., 2015. Observation of a new type of low-frequency waves at comet 67P/Churyumov-Gerasimenko. Annales Geophysicae, in press .

Rotundi, A., Sierks, H., Della Corte, V., Fulle, M., Gutierrez, P.J., Lara, L., Barbieri, C., Lamy, P.L., Rodrigo, R., Koschny, D., Rickman, H., Keller, H.U., López-Moreno, J.J., Accolla, M., Agarwal, J., A'Hearn, M.F., Altobelli, N., Angrilli, F., Barucci, M.A., Bertaux, J.L., Bertini, I., Bodewits, D., Bussoletti, E., Colangeli, L., Cosi, M., Cremonese, G., Crifo, J.F., Da Deppo, V., Davidsson, B., Debei, S., De Cecco, M., Esposito, F., Ferrari, M., Fornasier, S., Giovane, F., Gustafson, B., Green, S.F., Groussin, O., Grün, E., Güttler, C., Herranz, M.L., Hviid, S.F., Ip, W., Ivanovski, S., Jerónimo, J.M., Jorda, L., Knollenberg, J., Kramm, R., Kührt, E., Küppers, M., Lazzarin, M., Leese, M.R., López-Jiménez, A.C., Lucarelli, F., Lowry, S.C., Marzari, F., Epifani, E.M., McDonnell, J.A.M., Mennella, V., Michalik, H., Molina, A., Morales, R., Moreno, F., Mottola, S., Naletto, G., Oklay, N., Ortiz, J.L., Palomba, E., Palumbo, P., Perrin, J.M., Rodríguez, J., Sabau, L., Snodgrass, C., Sordini, R., Thomas, N., Tubiana, C., Vincent, J.B., Weissman, P., Wenzel, K.P., Zakharov, V., Zarnecki, J.C., 2015. Dust measurements in the coma of comet 67P/Churyumov-Gerasimenko inbound to the sun. Science 347. doi:`10.1126/science.aaa3905`.

Schmid, D., Volwerk, M., Plaschke, F., Vörös, Z., Zhang, T.L., Baumjohann, W., Narita, Y., 2014. Mirror mode structures near Venus and comet P/Halley. Annales Geophysicae 32, 651–657. doi:`10.5194/angeo-32-651-2014`.

Schulz, R., Hilchenbach, M., Langevin, Y., Kissel, J., Silen, J., Briois, C., Engrand, C., Hornung, K., Baklouti, D., Bardyn, A., Cottin, H., Fischer, H., Fray, N., Godard, M., Lehto, H., Le Roy, L., Merouane, S., Orthous-Daunay, F.R., Paquette, J., Rynö, J., Siljeström, S., Stenzel, O., Thirkell, L., Varmuza, K., Zaprudin, B., 2015. Comet 67P/Churyumov-Gerasimenko sheds dust coat accumulated over the past four years. Nature 518, 216–218. doi:`10.1038/nature14159`.

Snios, B., Lewkow, N., Kharchenko, V., 2014. Cometary emissions induced by scattering and fluorescence of solar X-rays. Astronomy & Astrophysics 568, A80. doi:`10.1051/0004-6361/201423769`.

Szego, K., Juhasz, A., Bebesi, Z., 2014. Possible observation of charged nanodust from comet 67P/Churyumov-Gerasimenko: An analysis for the ROSETTA mission. Planetary and Space Science 99, 48–54. doi:`10.1016/j.pss.2014.05.007`.

Utterback, M.G., Kissel, J., 1995. Interpretation of a glitch observed in the very small dust grain data at Halley's comet. Astrophysics and Space Science 225, 327–331. doi:`10.1007/BF00613246`.

Utterback, N.G., Kissel, J., 1990. Attogram dust cloud a million kilometers from comet Halley. The Astronomical Journal 100, 1315–1322. doi:`10.1086/115599`.

Winningham, J.D., Frahm, R.A., Sharber, J.R., Coates, A.J., Linder, D.R., Soobiah, Y., Kallio, E., Espley, J.R., Lundin, R., Barabash, S., Holmström, M., Andersson, H., Yamauchi, M., Grigoriev, A., Scherrer, J.R., Jeffers, S.J., Kataria, D.O., Kozyra, J.U., Luhmann, J.G., Roelof, E.C., Williams, D.J., Livi, S., Curtis, C.C., Hsieh, K.C., Sandel, B.R., Koskinen, H., Säles, T., Riihelä, P., Schmidt, W., Grande, M., Carter, M., Sauvaud, J.A., Fedorov, A., Thocaven, J.J., McKenna-Lawler, S., Orsini, S., Cerulli-Irelli, R., Maggi, M., Wurz, P., Bochsler, P., Krupp, N., Woch, J., Fränz, M., Asamura, K., Dierker, C., 2006. Electron oscillations in the induced martian magnetosphere. Icarus 182, 360–370. doi:`10.1016/j.icarus.2005.10.033`.